



## Following the electroreduction of uranium dioxide to uranium in LiCl–KCl eutectic *in situ* using synchrotron radiation



L.D. Brown<sup>a</sup>, R. Abdulaziz<sup>a</sup>, R. Jervis<sup>a</sup>, V.J. Bharath<sup>a</sup>, R.C. Atwood<sup>b</sup>, C. Reinhard<sup>b</sup>, L.D. Connor<sup>b</sup>, S.J.R. Simons<sup>a</sup>, D. Inman<sup>a</sup>, D.J.L. Brett<sup>a</sup>, P.R. Shearing<sup>a,\*</sup>

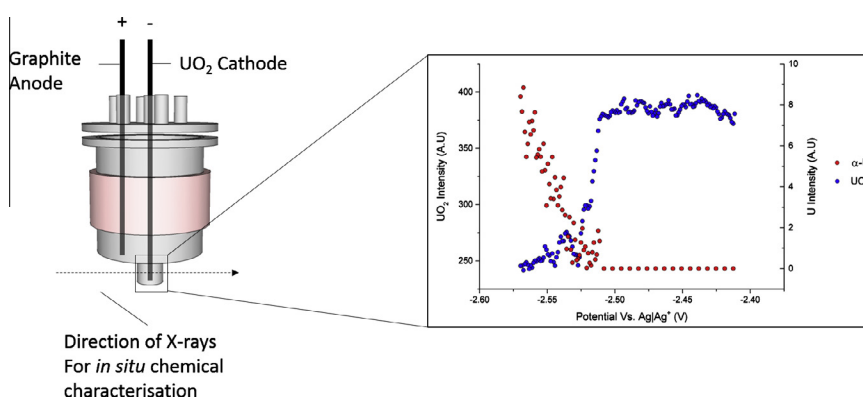
<sup>a</sup>Electrochemical Innovation Lab, Dept. Chemical Engineering, UCL, London WC1E 7JE, United Kingdom

<sup>b</sup>Diamond Light Source, Harwell Science and Innovation Campus, Didcot, Oxfordshire OX11 0DE, United Kingdom

### HIGHLIGHTS

- We investigated the electroreduction of  $\text{UO}_2$  to U in LiCl/KCl eutectic molten salt.
- Combined electrochemical measurement and *in situ* XRD is utilised.
- The electroreduction appears to occur in a single, 4-electron-step, process.
- No intermediate compounds were observed.

### GRAPHICAL ABSTRACT



### ARTICLE INFO

#### Article history:

Received 3 February 2015

Accepted 20 April 2015

Available online 28 April 2015

### ABSTRACT

The electrochemical reduction of uranium dioxide to metallic uranium has been investigated in lithium chloride–potassium chloride eutectic molten salt. Laboratory based electrochemical studies have been coupled with *in situ* energy dispersive X-ray diffraction, for the first time, to deduce the reduction pathway. No intermediate phases were identified using the X-ray diffraction before, during or after electroreduction to form  $\alpha$ -uranium. This suggests that the electrochemical reduction occurs via a single, 4-electron-step, process. The rate of formation of  $\alpha$ -uranium is seen to decrease during electrolysis and could be a result of a build-up of oxygen anions in the molten salt. Slow transport of  $\text{O}^{2-}$  ions away from the  $\text{UO}_2$  working electrode could impede the electrochemical reduction.

© 2015 The Authors. Published by Elsevier B.V. This is an open access article under the CC BY license (<http://creativecommons.org/licenses/by/4.0/>).

## 1. Introduction

Reprocessing of spent nuclear fuel has many benefits, including the recovery of valuable fissile material and the reduction in the radioactivity of nuclear wastes, which are conventionally stored in geological repositories [1]. Spent nuclear fuel reprocessing has traditionally utilised a liquid–liquid extraction (LLE) process route

for the separation of actinides, which has the notable drawback of poor proliferation resistance [2].

The ability to produce weapons grade material during reprocessing remains a significant barrier to widespread acceptance of nuclear power. Future technologies for spent fuel reprocessing must maintain proliferation resistance: electrochemical separations using molten salt electrolytes are promising candidate to achieve this [3].

Molten salt electrolytes have been proven to be a suitable media for the electrochemical separation of actinides; many studies have

\* Corresponding author. Tel.: +44 (0)20 7679 3783.

E-mail address: [p.shearing@ucl.ac.uk](mailto:p.shearing@ucl.ac.uk) (P.R. Shearing).

shown the ability to anodically titrate nuclear species into molten salts [4–9], to electroreduce/electrodeposit nuclear species from molten salts [5,10–15] and the ability to scale-up molten salt separation processes to the kg scale [16–18]. Inman et al. showed the electrochemical reversibility of  $U^{3+}|U$  system in LKE [5] and Sakamura et al. have shown the 4-electron transfer electroreduction process of  $UO_2$  to U in  $CaCl_2$  and  $LiCl$  salts [19]. In addition, molten salt electrolysis is also fundamental in the pyrochemical process developed in the USA [20–22]. This pyrochemical process utilises the electrolytic oxide reduction of  $UO_2$  to U in a  $LiCl$  salt containing  $Li_2O$  before the electrodeposition of U in a LKE electrorefiner. However, this electrolytic oxide reduction process may be negated by electrochemically reducing the  $UO_2$  in the electrorefiner prior to electroplating out the metal in the same unit.

To add, the electrochemical reduction of metal oxides to their metallic form is a function of the oxo-acidity of the molten salt system. For example, consider the simple 2-electron reduction of a metal oxide, MO, to its metallic form, M, forming the oxygen anion,  $O^{2-}$ :



Describing Eq. (1) using the Nernst equation yields the following:

$$E = E^0 + \frac{2.303RT}{2F} \log \left( \frac{a^{MO}}{a^M a^{O^{2-}}} \right) \quad (2)$$

where  $E$  is the cell potential,  $E^0$  is the standard cell potential,  $R$  is the universal gas constant,  $T$  is the temperature,  $F$  is the Faraday constant and  $a^x$  is the activity of species  $x$  ( $x = M, MO, O^{2-}$ ). From Eq. (2), it can be deduced that the electrochemical reduction potential is a function of the activity of oxide ions; consequently, a change in the oxo-acidity of the molten salt will affect the reduction potential. This effect may be predicted by the use of Predominance (also known as Littlewood) diagrams. These diagrams (which plot potential,  $E$ , versus the negative logarithm of the activity of  $O^{2-}$  ions,  $pO^{2-}$ ) serve as a useful tool for predicting metal–metal oxide–molten salt systems and have been widely applied for nuclear species in molten salt systems [23–26]. The Littlewood diagrams predict the electroreduction of  $UO_2$  to U to be a single, 4-electron-step, process, as shown in Fig. 1 [23]. However, to date there is limited experimental evidence to support this – indeed experiments tracking the reaction mechanism for the molten salt electroreduction of  $TiO_2$  to Ti (the FFC Cambridge process [27]) show a departure from the theory [28]. Although the

reduction of  $TiO_2$  to Ti metal using molten salts has recently been extensively investigated [27,29,30], *ex-situ* investigations led to much debate of the actual electrochemical reduction pathway [31,32], which seemed to differ from the thermodynamic predictions [33]. It was only after an *in situ* investigation using white beam synchrotron radiation that a detailed insight into the true electrochemical reduction pathway was obtained [28].

Here we aim to deduce the electrochemical reduction pathway of uranium dioxide to metallic uranium by combining electrochemical studies with *in situ* phase characterisation using synchrotron radiation.

## 2. Experimental

Two sets of experiments were carried out during this study; laboratory based electrochemistry and synchrotron based diffraction.

### 2.1. Laboratory experimental setup

Lithium chloride and potassium chloride salts (>99% purity, Sigma) were dried under vacuum at 175 °C for 72 h to remove residual water. Argon was administered into the vacuum oven to bring the pressure back to atmospheric pressure. The salts were then transferred, under argon, to a LABstar glove box workstation (MBraun) to be stored, ready for use. 100 g of LKE was used for all laboratory experiments. The working electrode assembly used was a metallic cavity electrode (MCE) which has been described elsewhere [34]. For reference, an electron micrograph of the MCE before and after electroreduction is shown in Fig. 2.

Uranium dioxide powder was produced in-house and was pressed into the MCE and attached to a molybdenum current collector, this assembly became the cathode. An approximate total of 0.04 mg of uranium dioxide powder is pressed into each hole of the MCE. A carbon rod of 3.05 mm  $\varnothing$  and 305 mm length (Alfa Aesar) was heated to remove any residual water and became the counter electrode. A saturated  $Cl^-$ , all-glass, silver–silver chloride reference electrode containing 0.75 mol  $kg^{-1}$   $AgCl$  was built and used as the reference electrode, as described elsewhere [35]. The salts were placed inside a 250 ml tall-form Pyrex beaker – known as the reaction vessel – which was then placed inside a custom-built Pyrex flanged tube – known as the safety envelope. The electrodes and gas inlet/outlet connections are held into a custom-built electrochemical cell head, made from Pyrophyllite – an

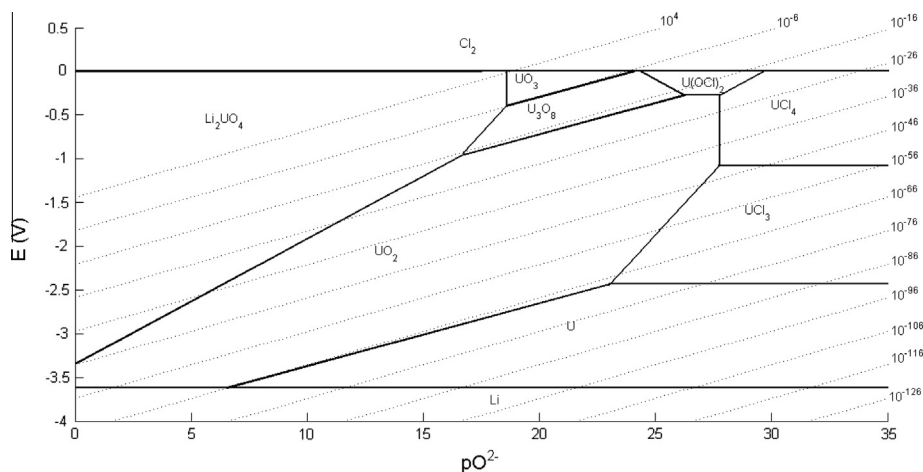
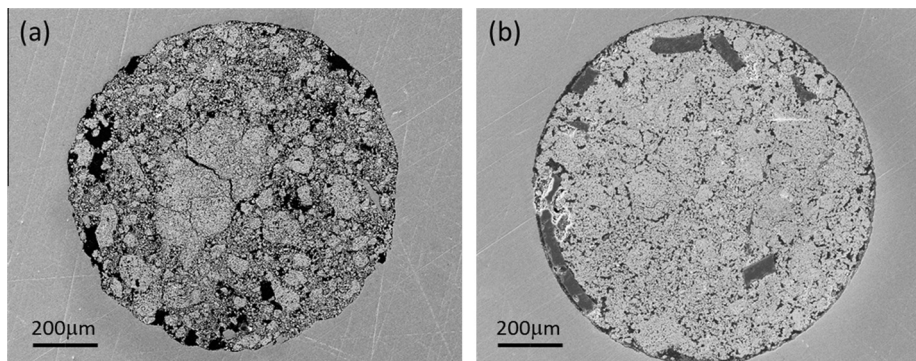


Fig. 1. Littlewood diagram for uranium species at unit activity in LKE. The potential ( $E$ ) is versus  $Cl^-|Cl_2$ . This diagram predicts the  $UO_2$  to U electroreduction pathway to be a single step process. Adapted from [23].



**Fig. 2.** Showing “birds-eye view” of separate metallic cavity electrodes (a) before and (b) after electrochemical reduction. The powder is pressed into 0.5 mm diameter holes which are drilled into 0.5 mm thick foils of molybdenum.

aluminium silicate – (Ceramic Substrates & Components Ltd.) and sealed with a metallic clamp. Research grade argon (99.9995% (<0.5 ppm O<sub>2</sub> and H<sub>2</sub>O)) was used in all experimentation. Glass was used in the laboratory experimental setup to ensure optical access into the cell, allowing for rapid identification of current process conditions (contamination of the melt, bubbles on electrodes, etc.). The heating source was a 5 L heavy duty Pyrex beaker loaded with 2 kg of an equimolar mixture of NaNO<sub>3</sub> and KNO<sub>3</sub> – known as the thermostatic salt bath. A custom built immersion heater, powered by a variable AC transformer, was used to heat the thermostatic salt beyond its melting point (250 °C). Once the thermostatic salt bath was molten, the electrochemical cell (safety envelope containing the reaction vessel) was placed inside the thermostatic salt bath to the working temperature (450 °C). The temperature was recorded using a Pyrex glass sheathed K-type thermocouple which was located inside the molten salt. A schematic of the lab based experimental setup can be seen in Fig. 3. All electrochemical measurements were taken using an IVIUMStat potentiostat (IVIUM Technologies).

## 2.2. Synchrotron experimental setup

Energy Dispersive X-ray Diffraction (EDXD) measurements were taken on beam line I12 (JEEP) at Diamond Light Source in

the UK. This diffraction technique differs from conventional, angle-dispersive, X-ray diffraction as the lattice plane distance – or *d*-spacing – is derived by determination of the wavelength of the diffracted polychromatic photons, as opposed to being derived from the diffraction angle of monochromatic photons [36]. The diffraction angle may be kept constant by the use of a collimator. As a direct result of using a collimator to define a constant Bragg angle, a lozenge shaped gauge volume in space is defined whereby only photons that are scattered within this volume will be detected by the detector. Placing the sample within this gauge volume has an advantage of being able to eliminate the signal from balance-of-apparatus components (the electrochemical cell, for example) and ensures that a high signal-to-noise ratio from the working electrode is collected. This is a useful advantage when using small samples, such as MCEs, which are on the sub-milligram range. An aluminium electrochemical cell was used to house the molten salt and electrodes were custom built for this investigation. The cell incorporates a well at the bottom of the cell where the MCE working electrode is located; to reduce the beam path through the cell, thus, reducing the X-ray attenuation. The MCE was aligned so that the UO<sub>2</sub> filled hole was normal to the X-ray beam. For investigations at the synchrotron, the electrochemical cell was loaded with 300 g of LKE inside an argon filled glove box (<0.1 ppm O<sub>2</sub> and H<sub>2</sub>O) (MBraun) and sealed with a

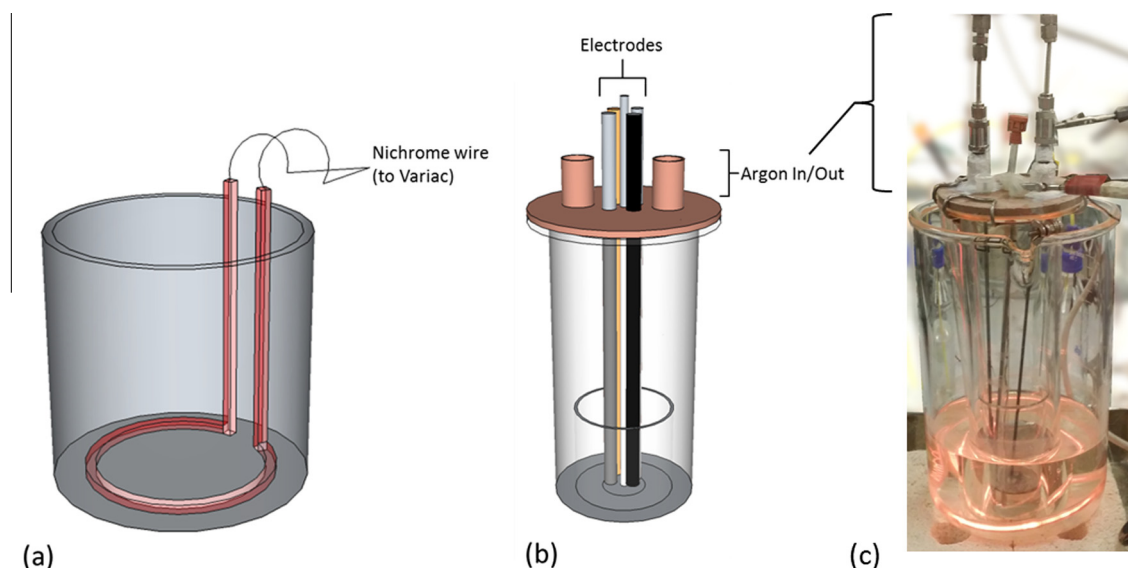


**Fig. 3.** Schematics of (a) the thermostatic salt bath furnace into which the electrochemical cell (b) is placed. Figure (c) is a photograph of the experimental setup in the laboratory.

stainless steel cell head with a graphite gasket. The cell head incorporated check valves on the gas in and out lines to ensure an airtight environment during transportation to the beam line and allowed a flow of inert gas into the cell during the investigations. Heating was supplied via a heating jacket and electrochemical measurements were taken using the aforementioned potentiostat. The cell was attached to the sample stage via a clamp which was bolted onto the sample stage. The sample stage allowed translations in three dimensions with a 10  $\mu\text{m}$  resolution. This ensured that the cell could be aligned in each direction by remotely moving the stage; the MCE was aligned in the X and Y directions using an X-ray imaging detector (which was moved during EDXD measurements). Z-direction alignment involved aligning the middle of the MCE into the middle of the gauge volume of the detector by measuring the signal-to-noise ratio of  $\text{UO}_2$  at different Z positions.

During the experimentation, a  $0.3 \times 0.3$  mm white X-ray beam of energies ranging from 45 to 150 keV irradiated a single  $\text{UO}_2$ -filled cavity on the MCE working electrode, inside the electrochemical cell. EDXD data was collected with a cryogenically cooled 23-element, high-purity, germanium detector (Canberra Industries, Inc.). The 23 detector elements are spaced every  $8.18^\circ$ , allowing azimuthal angles from  $0^\circ$  to  $180^\circ$  to be covered. The EDXD data collection was synchronised with the electrochemical measurements using an exposure time of 60 s. The take-off angle of  $4.5^\circ$  is defined by the collimator; all other X-rays which are diffracted at angles not equal to  $4.5^\circ$  are not detected. The collected diffraction patterns over the 23 elements were then averaged to produce a powder averaged diffraction pattern, improving the quality of the gathered data. The resulting EDXD data are plotted as a function of the photon energy of the diffracted X-rays, in contrast to powder X-ray diffraction data. These are obtained at a single wavelength and are plotted as a function of the scattering angle,  $2\text{-}\theta$ . A schematic of the electrochemical cell and the I12 setup can be seen in Fig. 4.

### 3. Results and discussion

#### 3.1. $\text{UO}_2$ precursor phase identification

The uranium dioxide precursor was first analysed using powder diffraction on a lab based X-ray diffractometer (STADI P, STOE & Cie GmbH). The powder X-ray diffraction pattern can be seen in Fig. 5. A full Rietveld analysis of this data yielded a cubic lattice

parameter of 5.465 Å. The error of this Rietveld analysis is displayed as a difference plot underneath Fig. 5a. This value for the lattice parameter is comparable to the cubic lattice parameter of 5.468 Å obtained by both Barrett et al. and Desgranges et al. [37,38]. In order to obtain the energies at which diffraction peaks for  $\text{UO}_2$  would be expected in the EDXD diffractogram, the XRD data was converted from a function of  $2\text{-}\theta$  to a function of energy using Bragg's law with a fixed angle of  $4.5^\circ$ .

This results in Fig. 5b and shows at which energy one would expect to see peaks for uranium dioxide, given a constant angle of  $4.5^\circ$ .

The X-ray energies for the four most prominent peak intensities of uranium dioxide were extracted and are tabulated in Table 1.

EDXD data of an empty MCE working electrode and one packed with  $\text{UO}_2$  were measured using the same beam line setup to validate the peak intensities calculated and to confirm the beam placement on the small MCE sample.

Fig. 6 shows EDXD diffractograms of an empty MCE (a) and one filled with  $\text{UO}_2$  (b). Referring back to Table 1, one can see that the peaks for  $\text{UO}_2$  are missing from Fig. 6a, as expected. However, peaks are present at 49.61, 57.37, 81.05 and 95.05 keV when the MCE was loaded with  $\text{UO}_2$  powder. The difference between these values and those calculated in Table 1 are due to changes in the  $d$ -spacing caused by the difference in temperature in which both data sets were collected. It should be noted that there are tungsten fluorescence peaks at  $\text{W } K_{\alpha 1} = 58.00$ ,  $\text{W } K_{\alpha 2} = 59.33$  and  $\text{W } K_{\beta 1} = 67.24$  keV (due to tungsten instrument shielding) which overlap with the (002)  $\text{UO}_2$  peak at 58.12 keV. Also, lead fluorescence peaks are present at  $\text{Pb } K_{\alpha 1} = 74.98$ ,  $\text{Pb } K_{\alpha 2} = 72.81$  and  $\text{Pb } K_{\beta 1} = 84.87$  keV which are, again, due to shielding of instruments. This phase identification allowed for rapid recognition of  $\text{UO}_2$  powder during alignment in the Z direction.

#### 3.2. Lab-based electrochemical characterisation

Pre-electrolysis of the molten salt electrolyte was performed to remove contaminants: a potential 200 mV more positive than the cathodic electrolyte decomposition potential was maintained for 2 h prior to all electrochemical measurements. Subsequently, the  $\text{UO}_2$  MCE ( $\sim 0.12$  mg  $\text{UO}_2$ ) was inserted into the molten salt and made the cathode. Cyclic voltammetry was performed between  $-1.9$  V and  $-2.6$  V, the onset potential of decomposition of the

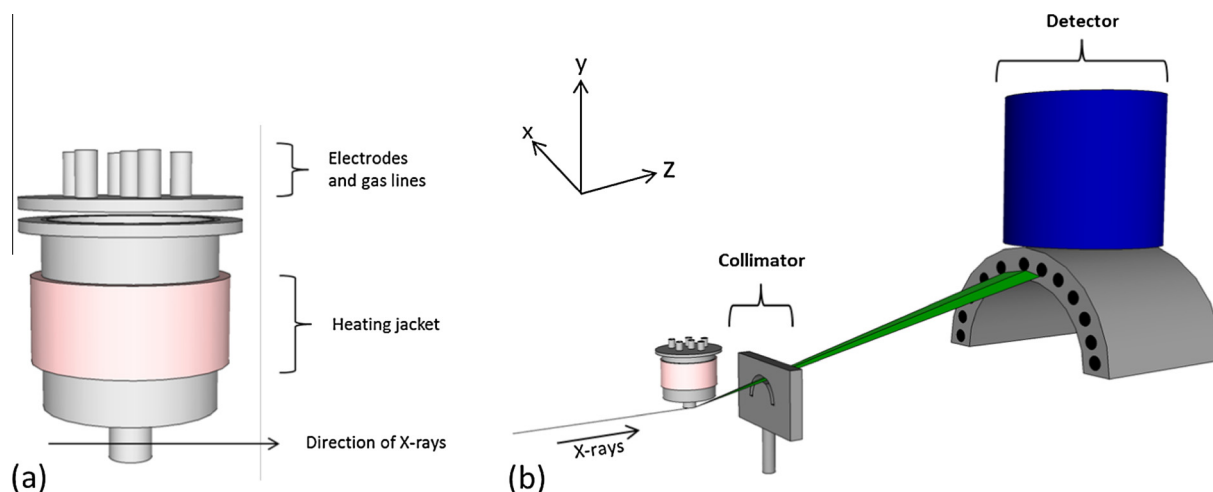


**Fig. 4.** (a) Electrochemical cell used for experimentation on I12 at Diamond Light Source. The cell is constructed from aluminium and incorporates a “well” at the bottom of the cell. The working electrode is positioned inside the well to ensure low attenuation of the X-ray beam. Figure (b) shows the experimental setup at the I12 JEEP beamline. Only X-rays (green) which are diffracted at  $4.5^\circ$  are detected by the individual elements on the EDXD detector (black circles). (For interpretation of the references to color in this figure legend, the reader is referred to the web version of this article.)

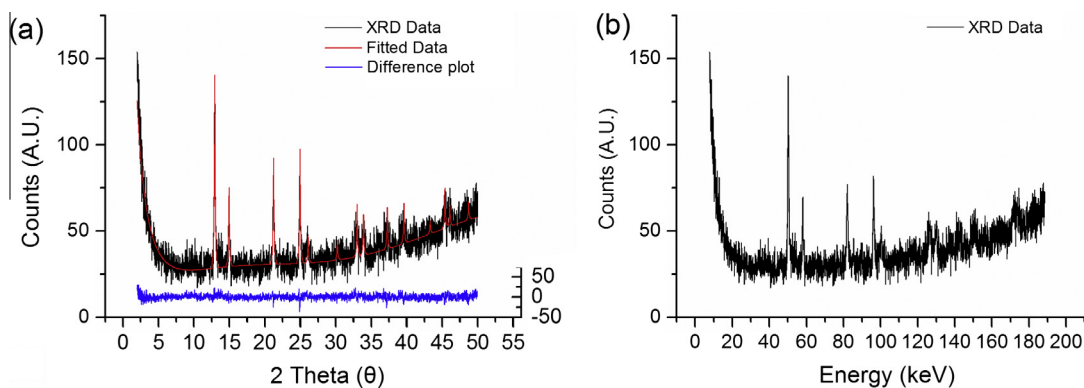


**Fig. 5.** X-ray diffractogram of  $\text{UO}_2$  powder showing: (a) the measured powder diffraction pattern (black), the Rietveld fit (red) and the difference plot (blue). The difference plot is the difference between the fitted data points and the observed data points. Figure (b) shows the raw data plot after conversion, as a function of energy. (For interpretation of the references to color in this figure legend, the reader is referred to the web version of this article.)

**Table 1**

Shows the powder X-ray diffraction angle and the calculated X-ray energies for the crystal planes shown.

Crystal plane ( <i>hkl</i> )	<i>d</i> -Space (Å)	Diffraction angle ( $2\theta$ )	X-ray energy (keV)
111	3.1	12.96	50.24
002	2.72	14.96	58.12
022	1.93	21.22	82.10
113	1.65	24.951	96.17

molten salt, with respect to the saturated  $\text{Cl}^-$   $\text{Ag}|\text{AgCl}$  reference electrode.

Fig. 7 shows a cyclic voltammogram of the  $\text{UO}_2$  MCE in LKE and contains four peaks labelled C1, C2, A1 and A2. The current has not been normalised to current density due to difficulties in efficiently assessing the immersed surface area in the cell for different electrodes. The electroreduction peak potential is close to the onset

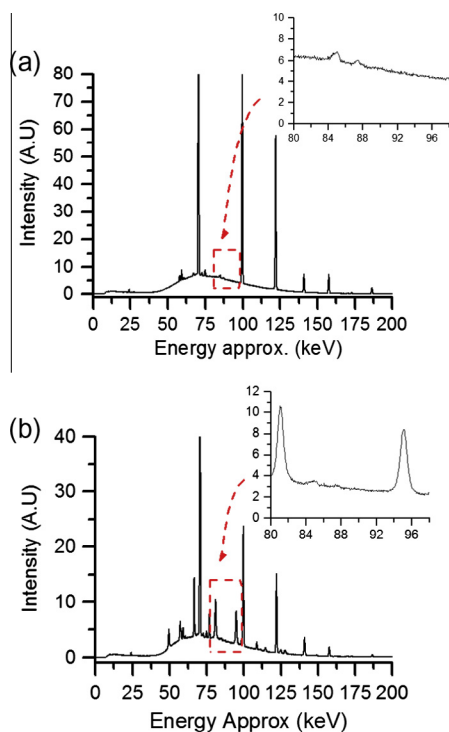


**Fig. 6.** EDXD diffractograms of (a) an empty MCE and (b) a  $\text{UO}_2$  filled MCE. The insets in each figure show, in detail, the region between 80 and 98 keV at which peaks for  $\text{UO}_2$  were expected.

potential of lithium decomposition of the molten salt; therefore the inflection point (*P*) is taken as the point of maximum current. Peak C1 – on the cathodic sweep – is attributed to the single, 4-electron-step, electrochemical reduction of uranium dioxide to uranium:



This is in agreement with Sakamura et al. who also observed the 4-electron reduction of uranium dioxide to uranium in both calcium chloride and lithium chloride molten salts [19].

Peak C2, is attributed to the decomposition of the LKE melt. That is, electrochemical plating of lithium onto the working electrode:



The absence of the re-oxidation peak (reverse of Eq. (4)) is due to the deposited lithium chemically reducing the  $\text{UO}_2$  to U via the following [39]:



$\text{Li}_2\text{O}$  is soluble in LKE and so once it is formed it would dissolve into the molten salt, causing the absence of the peak for lithium dissolution. Peak A1, on the anodic sweep, is attributed to

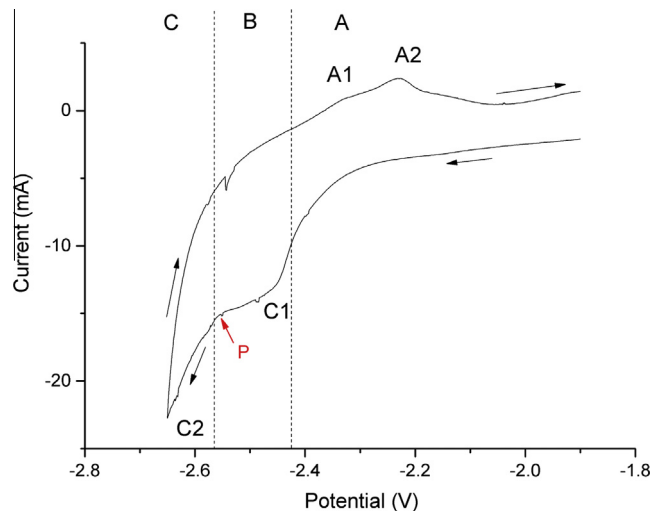


**Fig. 7.** Cyclic voltammogram versus  $\text{Ag}|\text{Ag}^+$  reference of  $\text{UO}_2$  filled MCE working electrode at 10 mV/s. The CV has been divided into three regions, moving in the negative potential direction: region A shows the current response before the electrochemical reduction; region B defines the potential range for the electrochemical reduction and region C depicts potentials more negative of the cathodic decomposition potential of the molten salt. Point *P* defines the inflection current.

oxidation of uranium. The charge passed is less than that at peak C1: 18.9 mC was passed on the cathodic sweep compared to 1.3 mC on the anodic sweep, A1. This discrepancy is thought to be due to the fact that some of the oxygen anions that were liberated during the electroreduction reaction have diffused away from the electrode and are not readily available at the MCE again for oxidation on the anodic sweep. Peak A2 is attributed to an oxidation of the molybdenum current collector. Because the surface area of the current collector is much greater than that of the MCE, oxide anions would be more readily available to react with the current collector compared to the MCE. The absence of a molybdenum reduction peak supports this; the molybdenum is oxidised after  $O^{2-}$  ions are liberated during the reduction of uranium dioxide.

### 3.3. In situ EDXD characterisation

Energy dispersive X-ray diffraction patterns were taken of the  $UO_2$  working electrode ( $\sim 0.12$  mg  $UO_2$ ) before, during and after all electrochemical measurements at 450 °C. Linear sweep voltammetry (LSV) was used for electrochemical reduction to allow for the electrochemical pathway to be deduced at multiple potentials. A LSV sweep rate of  $0.1$  mV  $s^{-1}$  was applied from a potential of  $-2.41$  V to  $-2.57$  V with respect to the Ag|AgCl reference. This slow sweep rate was utilised to help capture processes during the EDXD measurements. EDXD data were acquired during the entire LSV process with an integration time of 60 s per scan point. Analyses of the obtained diffraction patterns clearly show the electrochemical reduction of uranium dioxide to uranium in lithium chloride potassium chloride eutectic. The electroreduction appears to occur via a single, 4-electron, step and no intermediate products were observed. Uranium metal possesses three crystalline modifications;  $\alpha$ ,  $\beta$  and  $\gamma$  [40]. The  $\alpha$  phase is stable up to a temperature of 660 °C, the  $\beta$  phase is stable from 660 to 760 °C whilst the  $\gamma$  phase is stable from 760 to 1312 °C – its melting point. Le Bail refinement proved that the uranium phase formed during the electroreduction was  $\alpha$ -uranium, as expected.

Fig. 8a shows the peak intensity of different crystal planes of the uranium dioxide phase. From  $-2.41$  V to  $-2.43$  V (region A in Fig. 7), no electrochemical reaction occurs, as expected, and so there is no change in peak intensity. However, when the working electrode reaches a potential of  $-2.51$  V (region B in Fig. 7) a reduction in the peak intensity of uranium dioxide for all crystal planes is observed. Concurrently, a signal for uranium metal is recorded (Fig. 8b), in accordance with Eq. (3). The reduction in peak intensity of  $UO_2$  and sudden increase in U peak intensity can be easily observed in Fig. 8c. As the potential becomes more cathodic, the peak intensities for  $UO_2$  continue to reduce and those for uranium – specifically the 002 plane – continue to increase. This is indicative of the electrochemical reduction as the potential is within the  $UO_2|U$  electroreduction regime, as shown in Fig. 1. The rate of decrease of the peak intensities seems to decrease from within the potential range of  $-2.53$  to  $-2.56$  V as compared to the potential range of  $-2.51$  to  $-2.53$  V. It is expected that the reduction is curtailed at this point due to an increase in the concentration of  $O^{2-}$  ions in the melt, formed as a by-product of the reduction of  $UO_2$  (Eq. (3)). Due to the working electrode being positioned in the well of the aluminium cell, the transport of oxygen anions from cathode to anode would be more impeded compared to the laboratory setup in which the anode and cathode are in close proximity.

For example, assume that half (0.02 mg) of the  $UO_2$  inside the MCE was electrochemically reduced; this would relate to a molality in the molten salt of  $1E-04$  mol  $kg^{-1}$  of  $O^{2-}$  ions liberated during electroreduction. If this concentration of oxygen anions was not consumed at the counter electrode (as no  $O^{2-}$  ions are available to react the potential of the counter electrode is adjusted by the potentiostat to evolve  $Cl_2$  gas, ensuring two half-cell reactions occur) then

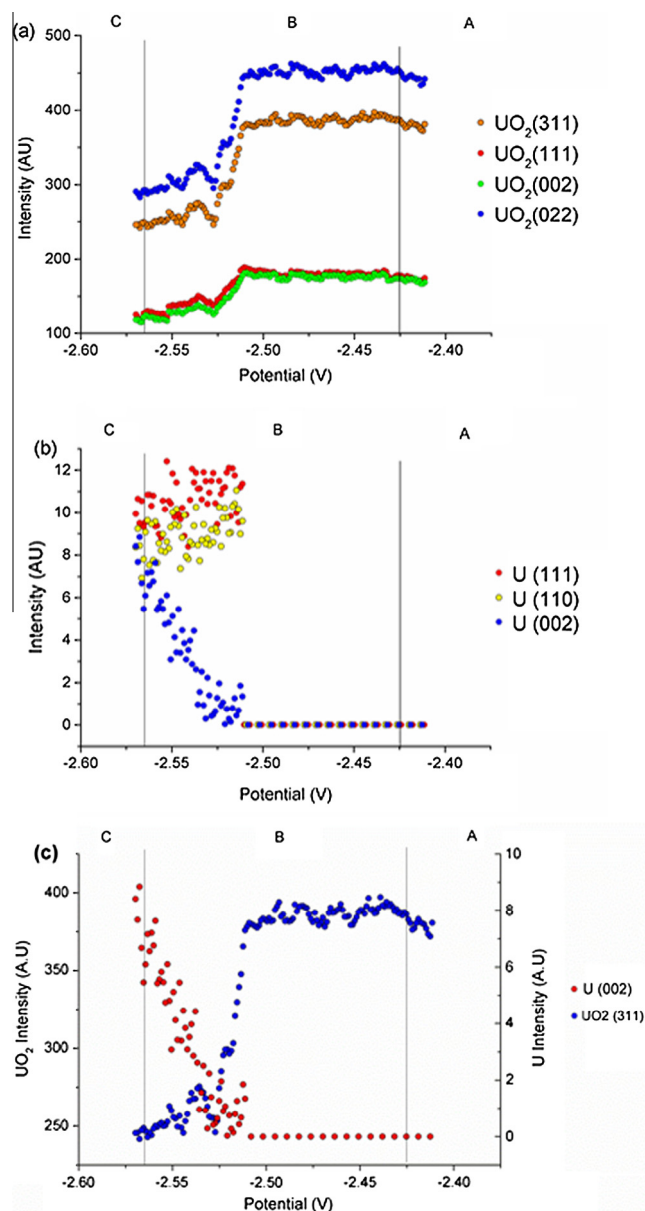


Fig. 8. (a) Peak intensities versus potential ( $0.1$  mV  $s^{-1}$ ) for uranium dioxide, (b) alpha uranium and (c) U (002) and  $UO_2$  (311) planes. Regions A–C (as defined in Fig. 7) are shown on all graphs.

this would result in a  $pO^{2-}$  value of 3.35. The electrochemical reduction is predicted to not be possible at this level of  $pO^{2-}$  (see Fig. 1 [23]) and could explain the discontinuation of electrochemical reduction. The geometry of the microstructure of the electrode could play an important role in this. Say the microstructure contains a highly tortuous pore phase; this would impede the transport of  $O^{2-}$  ions from the cathode to the anode, affecting the local activity of oxide ions and, thus, the level of  $pO^{2-}$ .

Table 2 shows the calculated lattice parameters for both  $UO_2$  (before electroreduction) and  $\alpha$ -uranium deduced from the Le Bail refinement analysis of the EDXD data. The difference in our calculated lattice parameters and derived cell volumes to those referenced in Table 2 are attributed to the difference in temperature at which these diffraction patterns were gathered: the thermal expansion of  $UO_2$  may be described by the following [42]:

$$L = L_{273}(9.9734 \times 10^{-1} + 1.179 \times 10^{-6}(T) - 2.705 \times 10^{-10}(T) + 4.391 \times 10^{-13}(T)) \quad (6)$$

**Table 2**

Calculated and reference values for the lattice parameters and cell volumes for uranium dioxide and uranium.

	Calculated lattice parameter { <i>abc</i> } at 703 K (Å)	Reference lattice parameter at 298 K { <i>abc</i> } (Å)	Calculated cell volume at 703 K (Å <sup>3</sup> )	Reference cell volume at 298 K (Å <sup>3</sup> )
UO <sub>2</sub>	5.488	5.468 [38]	165.32	163.49 [38]
α-U	{2.88 5.88 4.98}	{2.854 5.87 4.955} [41]	84.33	83.01 [41]

Eq. (6) predicts a thermal expansion of 0.4% for UO<sub>2</sub> at 703 K compared to that at 273 K. This is comparable to the 0.36% change seen in Table 1 for the lattice parameter for UO<sub>2</sub>.

#### 4. Conclusions

To conclude, the electrochemical reduction of uranium dioxide to uranium metal has been studied in a lithium chloride–potassium chloride eutectic molten salt at 450 °C. Both electrochemical and synchrotron X-ray techniques have been utilised to deduce the electrochemical reduction potential, mechanism and reduction pathway. The electrochemical reduction potential of the UO<sub>2</sub>|U couple is dependent on the activity of oxide ions existing within the melt. The electrochemical reduction of uranium dioxide to uranium metal seems to occur in a single, 4-electron-step, process; indicated by a single reduction peak (C1) in the cyclic voltammograms and also by the exclusion of any other phases in the EDXD data. The electrochemical reduction may be impeded by an increase in oxo-acidity of the molten salt. That is, O<sup>2-</sup> ions that are liberated by the electroreduction may not react at the counter electrode and, thus, not be removed from the molten salt. This could be due to the electrode geometry and/or the inherent microstructure of the working electrode: a high tortuosity, for example, would impede the diffusion of O<sup>2-</sup> ions out of the working electrode. This could then cause an increase in the activity of oxide ions existing within the melt and hence inhibit the electrochemical reduction – exploration of the microstructure of working electrodes will be the focus of future work.

#### Acknowledgements

This work was carried out as part of the UK Engineering and Physical Sciences Research Council (EPSRC) funded REFINE consortium (<http://www.refine.eng.ed.ac.uk/>). We gratefully acknowledge this EPSRC financial support (EP/J000531/1). We thank Diamond Light Source for access to beamline I12 (EE9690-1) that contributed to the results presented here. PRS thanks the Royal Academy of Engineering for financial support. We dedicate this publication to the memory of Professor Douglas Inman.

#### References

- [1] P. Taxil, L. Massot, C. Nourry, M. Gibilaro, P. Chamelot, L. Cassayre, J. Fluorine Chem. 130 (2009) 94–101.
- [2] J. McKibben, Radiochim. Acta 36 (1984) 3–16.
- [3] H.P. Nawada, K. Fukuda, J. Phys. Chem. Solids 66 (2005) 647–651.
- [4] F. Kobayashi, T. Ogawa, M. Akabori, Y. Kato, J. Am. Ceram. Soc. 78 (1995) 2279–2281.
- [5] D. Inman, G.J. Hills, L. Young, J.O.M. Bockris, Trans. Faraday Soc. 55 (1959) 1904–1914.
- [6] D.L. Hill, J. Perano, R.A. Osteryoung, J. Electrochem. Soc. 107 (1960) 698–705.
- [7] Y. Sakamura, O. Shirai, T. Iwai, Y. Suzuki, J. Alloys Compd. 321 (2001) 76–83.
- [8] O. Shirai, T. Iwai, K. Shiozawa, Y. Suzuki, Y. Sakamura, T. Inoue, J. Nucl. Mater. 277 (2000) 226–230.
- [9] T. Ogawa, K. Minato, Pure Appl. Chem. 73 (2001) 799–806.
- [10] S.A. Kuznetsov, H. Hayashi, K. Minato, M. Gaune-Escard, J. Electrochem. Soc. 152 (2005) C203–C212.
- [11] Y. Sakamura, T. Hijikata, K. Kinoshita, T. Inoue, T. Storvick, C. Krueger, J. Roy, D. Grimmett, S. Fusselman, R. Gay, J. Alloys Compd. 271 (1998) 592–596.
- [12] P. Masset, D. Bottomley, R. Konings, R. Malmbeck, A. Rodrigues, J. Serp, J.P. Glatz, J. Electrochem. Soc. 152 (2005) A1109–A1115.
- [13] F. Gao, C. Wang, L. Liu, J. Guo, S. Chang, L. Chang, R. Li, Y. Ouyang, J. Radioanal. Nucl. Chem. 280 (2009) 207–218.
- [14] S.-H. Kim, D.-S. Yoon, Y.-J. You, S. Paek, J.-B. Shim, S.-W. Kwon, K.-R. Kim, H.-S. Chung, D.-H. Ahn, H.-S. Lee, J. Nucl. Mater. 385 (2009) 196–199.
- [15] R.O. Hoover, M.R. Shaltry, S. Martin, K. Sridharan, S. Phongikaroon, J. Nucl. Mater. 452 (2014) 389–396.
- [16] J.J. Laidler, Pyrochemical Recovery of Actinides, Argonne National Lab, IL (United States), 1993.
- [17] J.J. Laidler, J.E. Battles, W.E. Miller, J.P. Ackerman, E.L. Carls, Prog. Nucl. Energy 31 (1997) 131–140.
- [18] R.D. Pierce, JOM 45 (1993) 40.
- [19] Y. Sakamura, M. Kurata, T. Inoue, J. Electrochem. Soc. 153 (2006) D31–D39.
- [20] K. Goff, R. Benedict, K. Howden, G. Teske, T. Johnson, Proc. GLOBAL (2005).
- [21] R. Benedict, C. Solbrig, B. Westphal, T. Johnson, S. Li, K. Marsden, K. Goff, Adv. Nucl. Fuel Cycles Syst. (2007).
- [22] S.X. Li, S. Herrmann, K. Goff, M. Simpson, R. Benedict, Nucl. Technol. 165 (2009) 190–199.
- [23] L.D. Brown, R. Abdulaziz, S. Simons, D. Inman, D.J.L. Brett, P.R. Shearing, J. Appl. Electrochem. 43 (2013) 1235–1241.
- [24] C. Caravaca, A. Laplace, J. Vermeulen, J. Lacquement, J. Nucl. Mater. 377 (2008) 340–347.
- [25] G. Landresse, G. Duyckaerts, Anal. Chim. Acta 65 (1973) 245–247.
- [26] L. Martinot, G. Duyckaerts, Anal. Chim. Acta 66 (1973) 474–476.
- [27] G.Z. Chen, D.J. Fray, T.W. Farthing, Nature 407 (2000) 361–364.
- [28] R. Bhagat, D. Dye, S.L. Raghunathan, R.J. Talling, D. Inman, B.K. Jackson, K.K. Rao, R.J. Dashwood, Acta Mater. 58 (2010) 5057–5062.
- [29] D.T.L. Alexander, C. Schwandt, D.J. Fray, Acta Mater. 54 (2006) 2933–2944.
- [30] C. Schwandt, D.J. Fray, Electrochim. Acta 51 (2005) 66–76.
- [31] G.Z. Chen, D.J. Fray, J. Electrochem. Soc. 149 (2002) E455–E467.
- [32] K. Dring, R. Dashwood, D. Inman, J. Electrochem. Soc. 152 (2005) E104–E113.
- [33] K. Dring, R. Dashwood, D. Inman, J. Electrochem. Soc. 152 (2005) D184–D190.
- [34] G. Qiu, M. Qiu, D. Ma, X. Wang, X. Jin, G. Hu, Chen, J. Electrochem. Soc. 152 (2005) E328.
- [35] J.O.M. Bockris, G.J. Bockris, D. Hills, L. Inman, J. Sci. Instrum. 33 (1956) (1950) 438–439.
- [36] B. Kämpfe, F. Luczak, B. Michel, Part. Part. Syst. Charact. 22 (2005) 391–396.
- [37] S. Barrett, A. Jacobson, B. Tofield, B. Fender, Acta Crystallogr. Sect. B: Struct. Crystallogr. Cryst. Chem. 38 (1982) 2775–2781.
- [38] L. Desgranges, G. Baldinozzi, G. Rousseau, J.-C. Niepce, G. Calvarin, Inorg. Chem. 48 (2009) 7585–7592.
- [39] S.M. Jeong, H.-S. Shin, S.-S. Hong, J.-M. Hur, J.B. Do, H.S. Lee, Electrochim. Acta 55 (2010) 1749–1755.
- [40] C.W. Tucker, Acta Crystallogr. A 4 (1951) 425–431.
- [41] G. Lander, M. Mueller, Acta Crystallogr. Sect. B: Struct. Crystallogr. Cryst. Chem. 26 (1970) 129–136.
- [42] D.G. Martin, J. Nucl. Mater. 152 (1988) 94–101.